Angular Distribution of Surface-Enhanced Raman Scattering from Individual Au Nanoparticle Aggregates

Timur Shegai,* Björn Brian, Vladimir D. Miljković, and Mikael Käll

Department of Applied Physics, Chalmers University of Technology, 412 96, Göteborg, Sweden

ABSTRACT Nano-optical antennas based on plasmonic metal particles are well-known for their ability to dramatically concentrate electromagnetic energy. However, not much attention has been devoted to the directionality properties of nanoantennas. Here, we report on the angular distribution of surface-enhanced Raman scattering (SERS) emitted by isolated aggregates of gold nanoparticles. We find that most of the radiation appears at angles exceeding the critical angle of the air−glass interface supporting the aggregates, and we demonstrate that angle-resolved imaging can be used as a fast and facile method for determination of the three-dimensional orientation and symmetry of the nanoantenna.

KEYWORDS: nanoantenna · surface-enhanced Raman scattering · Fourier imaging

Compact metal nanoantennas supporting plasmon resonances are able to focus light to volumes well below the diffraction limit and, through reciprocity, amplify emission from subwavelength sources. These effects are the basis for a number of surface-enhanced spectroscopies, including surface-enhanced Raman scattering (SERS),[1,2] fluorescence[3,4] (SEF), and infrared absorption (SEIRA).[5] Nanoplasmonic antenna effects combined with resonance Raman amplification even lead to single molecule sensitivity in SERS.[6−9] A number of aspects determine how suitable a particular nanoantenna is for spectroscopy applications. First, the nanoantenna has to be a good receiver of the incident far-field radiation used for excitation. The efficiency of this process strongly depends on how well the excitation overlaps in energy and polarization with the local surface plasmon resonance, which implies that the orientation of the nanoantenna in relation to the incident field is a crucial parameter. In molecular spectroscopy applications that involve an emission process, such as SERS and SEF, the nanoantenna also has to be able to efficiently convert the evanescent molecular source-field to propagating far-field radiation. This highlights the importance of the position and orientation of the molecule(s) in relation to the nanoantenna. In addition, the emission frequency should match the resonance frequency of the nanoantenna. In SERS, the emission occurs at a Stokes shifted frequency, and it often turns out that the most efficient SERS systems are those for which a plasmon resonance of the antenna overlaps with both the emission and excitation frequencies of the Raman scattering process.[9,10] The polarization of the SERS emission has also been extensively studied. In the case of dimer nanoantennas, for example, the light was shown to be polarized along the dimer axis,[11,12] as anticipated from simple field-enhancement arguments.

The nanoantenna aspects of surface-enhanced spectroscopy discussed above have been studied for the past three decades and are now comparatively well understood. Recently, however, the interest in nanoantennas has broadened to encompass the possibility of directional control over light emission, for example by means of miniaturized Yagi-Uda[13−15] and metal nanowire antennas.[16,17] Here, we study the angular distribution of light emitted by individual Raman nanoantennas located at an air-glass interface using Fourier imaging and high numerical aperture (NA) optics. We show that the SERS emission from compact clusters of 80 nm gold nanoparticles (NPs) peaks sharply at the air−glass critical angle, as expected for subwavelength sources located close to an interface.[18,19] This result is of practical interest because many SERS experiments are conducted on solid interfaces, typically air−glass or water−glass, but with low NA objectives that are not capable of capturing this "forbidden" light. Further, we find that the SERS emission from dimer nanoantennas has the same directionality as the scattering from the

*Address correspondence to timurs@chalmers.se.

Received for review November 19, 2010 and accepted February 8, 2011.

Published online February 16, 2011
10.1021/nn1031406

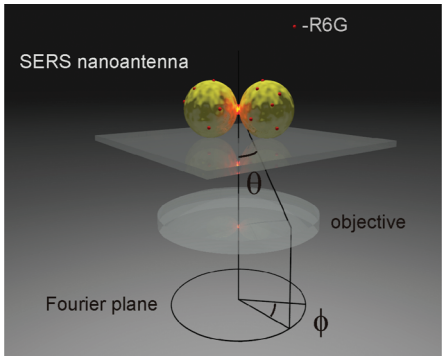

Figure 1. Scheme of the angle-resolved SERS detection. In the Fourier plane, the SERS intensity is distributed in a circle with the radial coordinate scaling as $r = \sin\theta$, and the tangential scaling as ϕ.

corresponding longitudinal dipolar dimer plasmon, despite the fact that both Raman excitation and emission overlaps with the transverse resonance of the nanoantenna. This surprising result highlights the importance of multipolar gap modes and the near-field aspect of the field-enhancement processes that is the basis for SERS.

RESULTS AND DISCUSSION

Figure 1 shows the principal arrangement of the experiment. The nanoantennas were formed by two or three aggregated NPs decorated with Rhodamine-6G (R6G) dye molecules, one of the strongest SERS molecules available. An aggregate was positioned within the field of view of the objective and excited by the laser. The scattered SERS photons were then collected by the same objective. The angular distribution of SERS radiation could be directly monitored in the Fourier plane of the optical microscope. It is useful to use cylindrical coordinates when describing the Fourier image so that the radial coordinate scales in proportion to $\sim\sin\theta$, and the tangential coordinate scales as ϕ, where θ and ϕ are defined in Figure 1.

Figure 2 summarizes the most important experimental observations. A dark-field (DF) image of an area was recorded; see Figure 2a. The same area was then used to collect a SERS image, which revealed a single intense spot in the region shown in Figure 2b. The position of the intense spot correlated well with the DF map. A *post situ* SEM image (Figure 2c) showed that the SERS signal originated from a dimer nanoantenna tilted with respect to the vertical axis. A SERS Fourier image is shown in Figure 2d. Note that the image is symmetric with respect to the dimer axis, depicted as a red dotted line in panel c. This means that Fourier imaging could be used for fast identification of the orientation of the nanoantenna. The green circle in the Fourier image indicates $NA_{max} = 1.3$ of the objective, which determines the maximum collection angle. The radial coordinate in the Fourier image is proportional to NA, so the position of the green circle unequivocally determines the angle θ in the Fourier

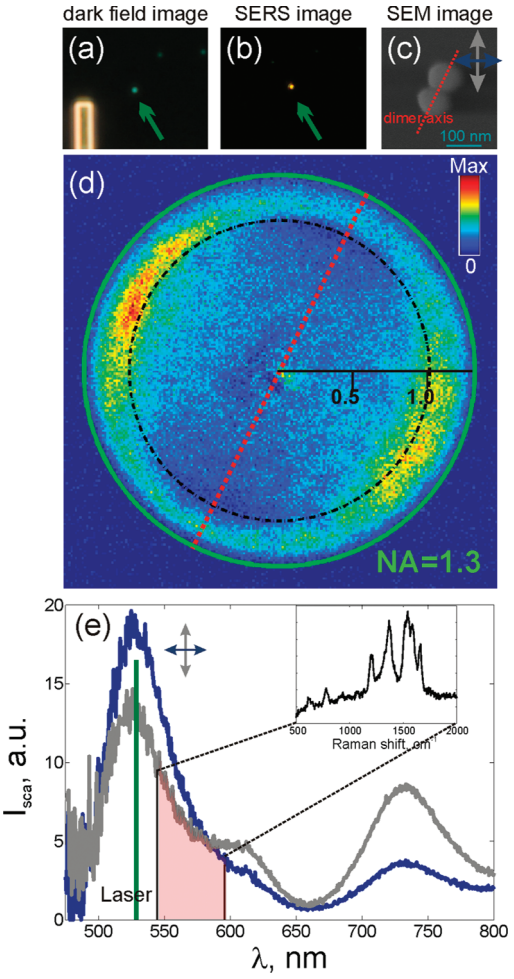

Figure 2. (a) Dark field image of a NP aggregate. (b) SERS image of the same area shown in panel a, green arrow indicates the position of the only intense spot in the area, which correlates well with the dark field image. (c) SEM image of the dimer nanoantenna. Gray and blue arrows indicate the directions of vertical and horizontal polarization. (d) Fourier image of SERS light emitted by the same NP aggregate. Note the symmetry with respect to the dimer axis. Green circle shows $NA_{max} = 1.3$ of the objective, black dash dot circle shows NA = 1, radial coordinate scales as NA. (e) Dark field spectra for horizontal and vertical polarizations. Spectra consist of two peaks, at ~530 and ~730 nm, which are due to transverse and longitudinal dipole plasmon resonances. The longitudinal component is larger for the vertical polarization, in accordance with the dimer orientation. Inset shows SERS spectrum of the dimer nanoantenna with characteristic R6G vibrational bands. Green line at $\lambda = 532$ nm indicates the position of the laser excitation, and red area to the right corresponds to the Raman region of 500−2000 cm^{-1} shown in the inset.

plane. To make reading of the Fourier data easier, we also show the position of NA = 1.0 and 0.5. Note that the most intense areas are observed at angles exceeding the critical angle ($\theta_c = 41.5°$ or NA = 1) for an air−glass interface. This is in perfect agreement with earlier works on dipole radiation near interfaces.[18,19] Two more dimers, showing similar dipole-like scattering behavior, are shown in Supporting Information, Figure S1.

Dark-field spectra for vertical and horizontal polarizations are shown in Figure 2e. The two distinct peaks

in the spectra, at about ~530 and ~730 nm, can be assigned to the transverse and longitudinal dipole plasmon resonances in the dimer, respectively.[20] The longitudinal resonance, which corresponds to charge oscillations along the dimer axis, is stronger for the vertical polarization, in accordance with the dimer orientation determined from SEM and Fourier imaging. The inset in panel e shows the SERS spectrum of the nanoantenna, exhibiting the characteristic vibrational modes of R6G.[21] The flat background underlying the SERS spectrum is probably dominated by enhanced fluorescence, although a Raman continuum might also contribute.[22,23]

Figure 3 shows experimental observations for a second nanoantenna. Again, at first a DF image of an area was recorded (Figure 3a). There was only one NP aggregate in the area, which also produced an intense SERS signal (Figure 3b). A SEM image of the nanoantenna showed that it was a trimer (Figure 3c). The corresponding SERS Fourier image is shown in Figure 3d. The fact that the axial symmetry is lost in a trimer in comparison to a dimer nanoantenna is reflected in the Fourier image. That is because in a symmetric trimer, like the one shown in Figure 3c, there are three junctions between the adjacent NPs, with each junction corresponding to an electromagnetic hot spot. Since there are about 10000 R6G molecules per one NP (see Methods section), it is very likely that all of these hot spots are populated with molecules and therefore are SERS active. To a first approximation, a trimer can therefore be thought of as a combination of three noninteracting dimers that each contributes an orientation sensitive Fourier image similar to the single dimer above. However, adding up three oriented Fourier images results in a circularly symmetric image, exactly as shown in Figure 3d. Again, the maximum radiation is observed at angles exceeding the critical angle. In reality, of course, three closely located NPs cannot be thought of as noninteracting. In fact, a trimer, in particular an asymmetric one, can exhibit a very peculiar wavelength dependent polarization behavior.[12,24,25] Fourier imaging is clearly a facile and potent experimental method to determine not only the orientation but also symmetry of a SERS nanoantenna. Figure 3e shows polarized DF spectra of the trimer nanoantenna. Similar to the dimer shown in Figure 2, the scattering spectra consist of two peaks, at ~530 and ~700 nm. In the trimer case, however, the intensity of the two spectra is nearly the same irrespective of polarization. This is in line with the trigonal symmetry of the nanoantenna and in agreement with previously published data.[26] As discussed in details in ref 26, there are six in-plane dipolar modes associated with the D_{3h} point symmetry group, with only four of them having nonvanishing dipole moment. Those four modes are in turn 2-fold degenerate and combine to produce two antibonding (high energy) and two bonding (low energy) normal modes, which give rise to the ~530 and ~700 nm peaks in the DF spectra, respectively. The inset in panel e shows the corresponding SERS spectrum of the trimer, again revealing the characteristic R6G vibrational pattern.

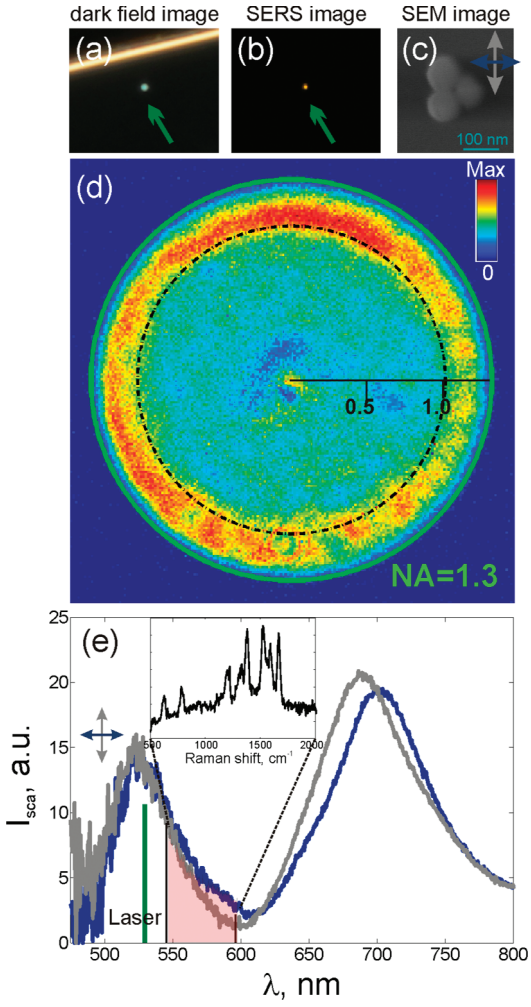

Figure 3. (a) Dark field image of a NP aggregate. (b) SERS image of the same area shown in panel a, green arrow indicates the position of the only intense spot in the area, which correlates well with the dark field image. (c) SEM image of the trimer nanoantenna. (d) SERS Fourier image. Note the circular symmetry around the center of the Fourier image. (e) Dark field spectra for horizontal and vertical polarizations. The spectra consist of two peaks, at ~530 and ~700 nm. The intensity of the two spectra is nearly the same irrespective of polarization, in contrast to the dimer case shown in Figure 2. Inset shows SERS spectrum of the trimer nanoantenna. Green line at λ = 532 nm indicates the position of the laser excitation and red area to the right corresponds to the Raman region of 500−2000 cm^{-1} shown in the inset.

An interesting observation can be made when considering the photon energies involved in the SERS and elastic scattering processes. First, note that the SERS signal is excited with circularly polarized light at 532 nm (see Methods section). The excitation wavelength (marked with a green line in Figures 2e and 3e) and the SERS emission (shown as a red region in Figures 2−3e) thus overlap with the transverse resonance of the

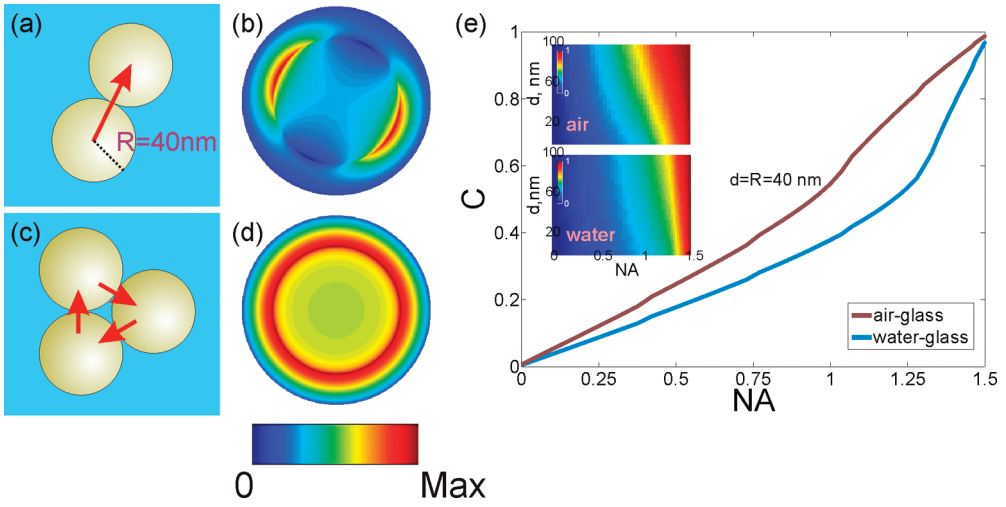

Figure 4. (a) Dimer aggregate oriented according to Figure 2c, red arrow, shows the direction of the dipole, located in the hot spot. Radius of the Au NP is $R = 40$ nm. (b) Fourier image of the dipole oriented according to panel a, radiating at $\lambda = 580$ nm and located at a distance $d = R = 40$ nm from the air-glass interface. (c) Trimer aggregate oriented according to Figure 3c, red arrows, shows the directions of three dipoles, each located at its hot spot in gaps between adjacent NPs. (d) Fourier image of three dipoles, shown in panel c, radiating at $\lambda = 580$ nm and located at a distance $d = R = 40$ nm from the air−glass interface. Note that the calculation is performed for incoherently radiating dipoles. (e) Collection efficiency, C, for a dipole radiation as a function of numerical aperture of the objective in the range of $0 < NA < 1.5$. The graphs are shown for air−glass and water−glass interfaces which are the most commonly used interfaces in microscopy experiments. Distance from the interface is taken to be $d = 40$ nm. Inset shows color-coded graphs for the collection efficiency as a function of distance ($0 < d < 100$ nm) for both kinds of interfaces. Geometrical factors in reference sphere approximation were used to calculate collection efficiencies.

dimer and the antibonding mode of the trimer, which both do not produce a high electric field in the junctions (see for example refs 26 and 27). However, the dipolar lobes seen in the Fourier SERS image of the dimer, Figure 2d, are oriented as if the source were a dipole polarized *parallel* to the dimer axis. This is surprising at first glance, because the photons involved in the Raman process are in resonance with the transverse dipolar plasmon mode, which is polarized *perpendicular* to the dimer axis! Therefore a high scattering intensity does not necessarily imply high local electric field amplification and *vice versa* (see, for example, ref 28). We take this observation as evidence for the crucial difference between the near-field and the far-field optical properties of the nanoantennas. SERS roughly scales as $\sim|E_{loc}|^4$ where E_{loc} is the local electric field at the position of the molecular emitter. Since there are about 10000 R6G molecules distributed over each NP in the present case, the contribution of each surface site to the SERS signal is simply determined by the fourth power of the local field enhancement at that particular site. Numerous studies have shown that the local field is strongest in narrow gaps between nanoparticles. But the field in a nanogap is polarized across the gap because the enhancement is mainly capacitive (electrostatic) in nature, which in turn implies that the dominant Raman "transition dipole" will be polarized parallel to the dimer axis. Further note that the capacitive gap field is in turn built up by a large number of evanescent multipolar plasmons that do not contribute to elastic scattering but have resonance energies that overlap the transverse dipolar dimer plasmon. Thus, elastic scattering in the 530−600 nm region is dominated by the transverse dipole mode, but the SERS emission is dominated by the local gap field, which is oriented along the dimer axis.

To further understand the angle-resolved SERS emission results, let us consider radiation of a Hertzian dipole near a planar interface. The electromagnetic field of an oscillating dipole contains near-, intermediate-, and far-field terms. In a homogeneous environment, only the far-field terms propagate to infinity, but when the dipole is placed very close to the interface, the near-field components, which exist above the interface, may be converted into propagating fields below the interface. Angles at which this occur are equal to or greater than the critical angle of the interface. This is described in detail in ref 29. The exact angular distribution of radiation depends on the orientation of the dipole, the distance between the dipole and the interface, and the wavelength of the emitted light. It is possible to simulate the Fourier image of a SERS nanoantenna, assuming that it radiates as a dipole, using analytical expressions from ref 19. We also assume that the dipole is parallel to the interface and the distance from the dipole to the interface (d) is equal to the radius of the gold NP used in the experiment ($R = 40$ nm). In other words, the dipole is assumed to be situated in the "hot spot" at the dimer junction. The wavelength is taken to be 580 nm, which corresponds to a Raman shift of 1550 cm^{-1} when excited at 532 nm (approximately the center of the SERS

spectrum, see insets of Figures 2e, 3e). Figure 4a shows the model for simulating the case of a dimer nanoantenna. The orientation of the dimer is kept as shown in Figure 2c. The red arrow shows the direction of the dipole corresponding to SERS radiation. Figure 4b shows that the computed Fourier image is in very good agreement with the experiment (Figure 2). In fact, the simulation reproduces essentially all important features of the experimental Fourier image, namely the symmetry with respect to the dimer axis and radiation at the critical angle. In Figure 4c, the model for the trimer nanoantenna is shown. Three "hot spots" of the trimer are assumed to radiate like three *incoherent* dipoles, shown as red arrows. Figure 4d shows the result of the simulation, which is again in excellent agreement with the experimental observation in Figure 3d.

The conversion of evanescent into propagating field components near an interface is the main process behind the angular distribution shown in Figure 4b,d. However, there is a secondary effect that is strictly due to geometrical reasons. In optical microscopy, the recorded far-field distribution measured by a flat detector originates from a spherical wave emitted by the source. This implies refraction of a spherical wave into a plane wave by means of the microscope's objective. To conserve energy along the various light paths of this refraction process, a geometrical parameter must be taken into account. In the so-called reference sphere approximation, the geometrical factor is equal to $1/\cos\theta$. Supporting Information, Figure S2a,c shows the reference sphere and a plot of $1/\cos\theta$ as a function of NA. Clearly this factor grows with NA (a factor of $\sim$3 for NA = 1.4), which makes the contribution of the light emitted at angles larger than the critical angle even larger. It is therefore very crucial to use high numerical aperture objectives for sensitive microscopy measurements, like for example single-molecule SERS or fluorescence. To illustrate this fact quantitatively, collection efficiencies for air−glass and water−glass interfaces are plotted in Figure 4e. The dipoles are assumed to be 40 nm away from the interface and radiate at 580 nm. The collection efficiency as a function of NA is calculated by first integrating the intensity inside a circle with radius of NA and then normalizing it with respect to the overall intensity emitted into the glass hemispace. Notice the increase in the rate of collection efficiency growth with increasing angle upon passing the critical angle (NA = 1 for air−glass and NA = 1.33 for water−glass interfaces). The inset shows the collection efficiencies for air− and water−glass interfaces computed at various distances from the dipole to the interface. The result indicates that it is especially important to use high NA objectives for emitters located very close to the water−glass interface. In Figure 4e, we used a reference sphere ($1/\cos\theta$) approximation for estimating the geometrical factor contribution; however, it is only a good approximation at low angles. In reality a spherical surface cannot refract a spherical wavefront, as it is shown in Supporting Information, Figure S2a, but instead an elliptical surface should be used (Supporting Information, Figure S2b). The geometrical factor due to the so-called reference ellipse approximation is larger than the corresponding reference sphere factor (see Supporting Information for details). In reality, commercial objective lenses are neither spherical nor elliptical surfaces, which means that the geometrical factor in real objectives should lie somewhere between those extreme cases (dashed area in Supporting Information, Figure S2c). The collection efficiencies shown in Figure 4e are therefore overestimated at high NAs, and so for real microscopy applications it is even more important to use high NA objectives.

In conclusion, we experimentally measured the angular distribution of Raman scattering emitted by individual dimer and trimer nanoantennas positioned on an air−glass interface. We observed that most of the light was emitted at angles exceeding the critical angle and that the overall Fourier images were highly sensitive to the orientation and symmetry of the nanoantenna. The data agreed extremely well with simple models based on isolated dipole emitters located close to an interface. The results further illustrated the crucial difference between near-field (SERS) and far-field (elastic scattering) properties of plasmonic nanoantennas. Finally, our findings demonstrated the importance of using high NA objectives in SERS studies of surface immobilized nanostructures using inverted microscopes.

METHODS

The nanoantennas were prepared from a colloidal suspension of monodisperse, citrate stabilized 80 nm gold NPs (BBI International). The NP suspension was mixed with a water solution of Rhodamine-6G (R6G) and NaCl to final concentrations of 0.01 nM NPs, 0.1 μM dye, and 10 mM salt. This means that there were of the order of 10000 R6G molecules per NP. The solution was allowed to incubate overnight. Excess of unadsorbed R6G molecules were removed by centrifugation at 500*g* for 10 min. The supernatant was then removed and the precipitate redissolved in 10 mM NaCl solution. Further, a drop of the solution containing gold NP aggregates was placed on a glass slide coated with polylysine (0.25 mg/mL water solution for 5 min) for 1 min. The slide was then thoroughly rinsed with Milli-Q water and dried under a stream of nitrogen. Before adsorbing nanoparticles, the glass slide was decorated with an indexed grid consisting of 50 μm gold triangles prepared by electron beam lithography (EBL), which facilitated *post situ* scanning electron microscopy (SEM) of a desired nanoantenna. All experiments were performed on air−glass interfaces.

Raman excitation was performed with a 532 nm laser at a power of 1 kW/cm^2 incident on the sample. Circular polarization was used in order to effectively excite randomly oriented nanoantennas. The sample was mounted on an XY stage of a Nikon Eclipse TE2000-E inverted microscope, equipped with a Nikon 100× NA = 0.7−1.3 oil immersion objective and illuminated in an epi-illumination fashion. The Rayleigh component was removed by a dichroic mirror and a long pass filter (Chroma). For dark field (DF) imaging and spectroscopy a 0.8−0.95 air dark field condenser (Nikon) with a polarizer was used, and the numerical aperture of the objective was set to 0.7. For SERS measurements, the numerical aperture was increased to 1.3. Both SERS and DF spectra were recorded by a fiber-coupled spectrometer (Andor, SR-303I-B), while color images were obtained by Nikon D300s DSLR camera. The angular distribution of the Raman scattered light was measured through Fourier imaging. Because the primary Fourier plane is situated inside the objective's body, it is only possible to record a conjugated Fourier plane by means of additional optics. We used a so-called 4*f* correlator, in which the lens system could be interchanged such that both direct images and Fourier images could be recorded on the same CCD detector (the scheme of the device is given in Supporting Information, Figure S3). All lenses were 1 in. achromats designed for the visible wavelength range.

Acknowledgment. We acknowledge financial support from the Göran Gustafsson Foundation, the Swedish Foundation for Strategic Research and the Swedish Research Council.

Supporting Information Available: Figures S1−S3 with additional text and formulas. This material is available free of charge *via* the Internet at http://pubs.acs.org.

REFERENCES AND NOTES

1. Jeanmaire, D. L.; Van Duyne, R. P. Surface Raman Spectroelectrochemistry. *J. Electroanal. Chem.* **1977,** *84*, 1–20.
2. Moskovits, M. Surface-Enhanced Spectroscopy. *Rev. Mod. Phys.* **1985,** *57*, 783–826.
3. Taminiau, T. H.; Stefani, F. D.; Segerink, F. B.; Van Hulst, N. F. Optical Antennas Direct Single-Molecule Emission. *Nat. Photonics* **2008,** *2*, 234–237.
4. Kinkhabwala, A.; Yu, Z. F.; Fan, S. H.; Avlasevich, Y.; Mullen, K.; Moerner, W. E. Large Single-Molecule Fluorescence Enhancements Produced by a Bowtie Nanoantenna. *Nat. Photonics* **2009,** *3*, 654–657.
5. Hartstein, A.; Kirtley, J. R.; Tsang, J. C. Enhancement of the Infrared-Absorption from Molecular Monolayers with Thin Metal Overlayers. *Phys. Rev. Lett.* **1980,** *45*, 201–204.
6. Kneipp, K.; Wang, Y.; Kneipp, H.; Perelman, L. T.; Itzkan, I.; Dasari, R.; Feld, M. S. Single Molecule Detection Using Surface-Enhanced Raman Scattering (SERS). *Phys. Rev. Lett.* **1997,** *78*, 1667–1670.
7. Nie, S. M.; Emory, S. R. Probing Single Molecules and Single Nanoparticles by Surface-Enhanced Raman Scattering. *Science* **1997,** *275*, 1102–1106.
8. Xu, H. X.; Bjerneld, E. J.; Käll, M.; Borjesson, L. Spectroscopy of Single Hemoglobin Molecules by Surface Enhanced Raman Scattering. *Phys. Rev. Lett.* **1999,** *83*, 4357–4360.
9. Schatz, G. C.Young, M. A.Van Duyne, R. P.Electromagnetic Mechanism of SERS. *Surface-Enhanced Raman Scattering: Physics and Applications*; Springer-Verlag: Berlin, 2006; Vol. 103, pp 19−45.
10. McFarland, A. D.; Young, M. A.; Dieringer, J. A.; Van Duyne, R. P. Wavelength-Scanned Surface-Enhanced Raman Excitation Spectroscopy. *J. Phys. Chem. B* **2005,** *109*, 11279–11285.
11. Xu, H.; Käll, M. Polarization-Dependent Surface-Enhanced Raman Spectroscopy of Isolated Silver Nanoaggregate. *ChemPhysChem* **2003,** *4*, 1001–1005.
12. Shegai, T. O.; Li, J.; Dadosh, T.; Zhang, Z.; Xu, H.; Haran, G. Managing Light Polarization *via* Plasmon-Molecule Interactions within an Asymmetric Metal Nanoparticle Trimer. *Proc. Natl. Acad. Sci. U.S.A.* **2008,** *105*, 16448–16453.
13. Curto, A. G.; Volpe, G.; Taminiau, T. H.; Kreuzer, M. P.; Quidant, R.; van Hulst, N. F. Unidirectional Emission of a Quantum Dot Coupled to a Nanoantenna. *Science* **2010,** *329*, 930–933.
14. Kosako, T.; Kadoya, Y.; Hofmann, H. F. Directional Control of Light by a Nano-optical Yagi-Uda Antenna. *Nat. Photonics* **2010,** *4*, 312–315.
15. Pakizeh, T.; Käll, M. Unidirectional Ultracompact Optical Nanoantennas. *Nano Lett.* **2009,** *9*, 2343–2349.
16. Li, Z. P.; Hao, F.; Huang, Y. Z.; Fang, Y. R.; Nordlander, P.; Xu, H. X. Directional Light Emission from Propagating Surface Plasmons of Silver Nanowires. *Nano Lett.* **2009,** *9*, 4383–4386.
17. Shegai, T.; Miljkovic, V. D.; Bao, K.; Xu, H. X.; Nordlander, P.; Johansson, P.; Käll, M. Unidirectional Broadband Light Emission from Supported Plasmonic Nanowires. *Nano Lett.* **2011,** *11*, 706–711.
18. Huang, C.; Bouhelier, A.; des Francs, G. C.; Bruyant, A.; Guenot, A.; Finot, E.; Weeber, J. C.; Dereux, A. Gain, Detuning, and Radiation Patterns of Nanoparticle Optical Antennas. *Phys. Rev. B* **2008,** *78*, 155407.
19. Lieb, M. A.; Zavislan, J. M.; Novotny, L. Single-Molecule Orientations Determined by Direct Emission Pattern Imaging. *J. Opt. Soc. Am. B* **2004,** *21*, 1210–1215.
20. Gunnarsson, L.; Rindzevicius, T.; Prikulis, J.; Kasemo, B.; Käll, M.; Zou, S.; Schatz, G. C. Confined Plasmons in Nanofabricated Single Silver Particle Pairs: Experimental Observations of Strong Interparticle Interactions. *J. Phys. Chem. B* **2005,** *109*, 1079–1087.
21. Weiss, A.; Haran, G. Time-Dependent Single-Molecule Raman Scattering as a Probe of Surface Dynamics. *J. Phys. Chem. B* **2001,** *105*, 12348–12354.
22. Xu, H. X.; Wang, X. H.; Persson, M. P.; Xu, H. Q.; Käll, M.; Johansson, P. Unified Treatment of Fluorescence and Raman Scattering Processes near Metal Surfaces. *Phys. Rev. Lett.* **2004,** *93*, 243002.
23. Johansson, P.; Xu, H. X.; Käll, M. Surface-Enhanced Raman Scattering and Fluorescence Near Metal Nanoparticles. *Phys. Rev. B* **2005,** *72*, 035427.
24. Li, Z. P.; Shegai, T.; Haran, G.; Xu, H. X. Multiple-Particle Nanoantennas for Enormous Enhancement and Polarization Control of Light Emission. *ACS Nano* **2009,** *3*, 637–642.
25. Shegai, T. O.; Haran, G. Probing the Raman Scattering Tensors of Individual Molecules. *J. Phys. Chem. B.* **2006,** *110*, 2459–2461.
26. Alegret, J.; Rindzevicius, T.; Pakizeh, T.; Alaverdyan, Y.; Gunnarsson, L.; Käll, M. Plasmonic Properties of Silver Trimers with Trigonal Symmetry Fabricated by Electron-Beam Lithography. *J. Phys. Chem. C* **2008,** *112*, 14313–14317.
27. Xu, H. X.; Aizpurua, J.; Käll, M.; Apell, P. Electromagnetic Contributions to Single-Molecule Sensitivity in Surface-Enhanced Raman Scattering. *Phys. Rev. E* **2000,** *62*, 4318–4324.
28. Le Ru, E. C.; Galloway, C.; Etchegoin, P. G. On the Connection between Optical Absorption/Extinction and SERS Enhancements. *Phys. Chem. Chem. Phys.* **2006,** *8*, 3083–3087.
29. Novotny, L.; Hecht, B., Dipole Emission Near Planar Interfaces. In *Principles of Nano-Optics*; Cambridge University Press: New York, 2006; pp 335−362.